# Exciton-Condensate-Like Amplification of Energy Transport in Light Harvesting

Anna O. Schouten, LeeAnn M. Sager-Smith, and David A. Mazziotti Department of Chemistry and The James Franck Institute, The University of Chicago, Chicago, Illinois 60637, USA

(Received 21 December 2022; revised 11 March 2023; accepted 20 March 2023; published 28 April 2023)

Bose-Einstein condensation of excitons, in which excitons condense into a single coherent quantum state, known as an exciton condensate, enables frictionless energy transfer, but typically occurs under extreme conditions in highly ordered materials, such as graphene double layers. In contrast, photosynthetic light-harvesting complexes demonstrate extremely efficient transfer of energy in disordered systems under ambient conditions. Here, we establish a link between the two phenomena by investigating the potential for exciton-condensate-like amplification of energy transport in room-temperature light harvesting. Using a model of the Fenna-Matthews-Olson complex and accounting for intrachromophore electron correlation explicitly through the addition of multiple sites to the individual chromophores, we observe amplification of the exciton population in the particle-hole reduced density matrix through an exciton-condensate-like mechanism. The exciton-condensate-like amplification evolves with the dynamics of exciton transfer, and the nature of amplification is influenced by intra- and interchromophore entanglement, as well as the initial excitation model and number of sites per chromophore. Tuning intrachromophore coupling also increases the rate of exciton transfer with a maximum enhancement of nearly 100%. The research provides fundamental connections between exciton condensation and exciton transport in light-harvesting complexes with potential applications for harnessing the exciton-condensate-like mechanism to enhance energy transfer in synthetic systems and create new materials capable of highly efficient energy transfer.

DOI: 10.1103/PRXEnergy.2.023002

### I. INTRODUCTION

Unlike electrons and holes, excitons—quasiparticles formed by electron-hole pairing—are bosons. Consequently, excitons can undergo Bose-Einstein-like condensation, a process whereby many excitons condense into a single quantum state [1-4]. Like other condensation phenomena, exciton condensation leads to superfluidity of the condensed particles, that is, superfluidity of excitons [5]. Because of the nature of excitons, rather than transferring charge or mass, superfluidity of excitons results in superfluid transfer of energy [6]. Despite the inarguable advantages that such transfer offers to discovering energyefficient systems, for many years, exciton condensation has remained elusive, as experimental realization of this effect is difficult, partly due to the short lifetimes of excitons. Excitons generally decay quickly by recombining, causing

Published by the American Physical Society under the terms of the Creative Commons Attribution 4.0 International license. Further distribution of this work must maintain attribution to the author(s) and the published article's title, journal citation, and DOI.

them to release the excitation energy. As such, exciton condensation typically requires extremely low temperatures or high magnetic fields to extend the excitonic lifetime [7,8], although recent literature has also shown condensation may be possible under more tractable conditions in bilayer structures [9,10] like bilayer graphene [11–14] and van der Waals heterostructures [15-20], where spatial separation helps to increase the excitonic lifetime by preventing recombination. Recent work has also shown the possibility for the beginnings of exciton condensation in small-scale molecular and quantum systems [21-25], suggesting an exciton-condensation-like mechanism could be possible in a small-scale system like a light-harvesting complex.

Photosynthetic light-harvesting complexes transfer energy with extremely high efficiency; thus, understanding the governing mechanisms in these systems is important for identifying general principles for efficient energy transfer. Such principles can then be applied to create highly efficient synthetic energy transfer systems. Lightharvesting complexes transfer energy in the form of excitons created by photoexcitation of an electron. Excitons are shuttled through a series of chromophores acting like energy-transferring wires to a reaction center, where the

<sup>\*</sup>damazz@uchicago.edu

energy can be collected for use in biological processes [26]. The structures and functions of light-harvesting complexes for exciton transfer are established in the literature, but over the last several decades much attention has been directed to understanding the role of quantum effects in exciton transfer. Indeed, there have been numerous studies probing the roles of dephasing [27–29], strong correlation [30–32], quantum coherence [33–36], and entanglement [37–41] in light-harvesting complexes. Both theoretical and experimental studies have established that quantum effects are present, and, while some debate remains as to the nature and role of these effects in the energy transfer process [36], there is evidence they could have significant implications for the design of synthetic energy transfer systems [31,42,43].

Because exciton condensation has thus far been demonstrated under such different conditions from exciton transfer in light-harvesting complexes (macroscopic materials at low temperatures, in contrast to microscopic biological systems under ambient conditions), the two phenomena are generally not connected in the literature, even though both are closely tied to efficient exciton transport. Here, we connect the two processes and explore energy transfer and exciton condensation in the Fenna-Matthews-Olson (FMO) [44-46] complex of green-sulfur bacteria using a theoretical model that explicitly introduces strong electron correlation in the form of intrachromophore coupling [30–32]. Similar to the introduction of strong intrachromophore coupling in Ref. [30], we expand the typical one-body model used for the FMO complex to a model with multiple electron sites on each chromophore, creating additional channels for exciton transfer. The coupling between the sites on the chromophores can be tuned using a coupling parameter, which we find influences the rate of exciton transfer through either constructive or destructive quantum interference, depending on the amount of coupling. Additionally, we show that the nature of the initial excitation state and the number of sites per chromophore have an effect on the rate of exciton transport. In connection to exciton condensation, the model exhibits a signature for exciton condensation in the single-excitation manifold. The signature, which evolves with the dynamics of exciton transport, results from a combination of interand intrachromophore entanglement and depends on the initial excitation and number of sites per chromophore. Initial conditions can be selected that maximize the signature within the single-excitation manifold for the specified number of sites per chromophore. The results demonstrate a link between the enhanced exciton transfer and the exciton-condensation-like mechanism, which may further elucidate efficient energy transfer. Understanding the possible connections between these two phenomena will provide insight into the exciton-condensation-like amplification that could assist in optimizing energy transfer in other systems.

### II. RESULTS AND DISCUSSION

Electron correlation in photosynthetic light-harvesting complexes is an important feature of the energy transfer process. Mazziotti [30] emphasizes this for the FMO complex, showing that electron correlation and entanglement within the chromophores significantly increases the efficiency of energy transfer by creating additional pathways or channels for transfer. This idea is represented in Fig. 1, which shows two sets of interacting intrachromophore units, each creating a potential path to the reaction center. Recent research [31] has reiterated the importance of intra-unit-cell delocalization to long-range energy transfer, showing that delocalization within unit cells allows for greater diffusion between states, and thus, faster energy transfer. Additionally, other recent research [32] demonstrated that intra-unit-cell coupling could improve energy transfer by limiting radiative recombination. We consider electron correlation by explicitly building intrachromophore coupling into our model to explore the impacts of such coupling on energy transfer in the contexts of exciton populations and entanglement.

Our coupled model is based on a one-body Hamiltonian used extensively in the study of FMO exciton transport dynamics [27–29,39,40,47], with site energies and interchromophore coupling parameters from the  $7 \times 7$  Hamiltonian matrix of Ref. [27]. We adapt the one-body model to create a correlated model by introducing additional degenerate sites to each chromophore that have

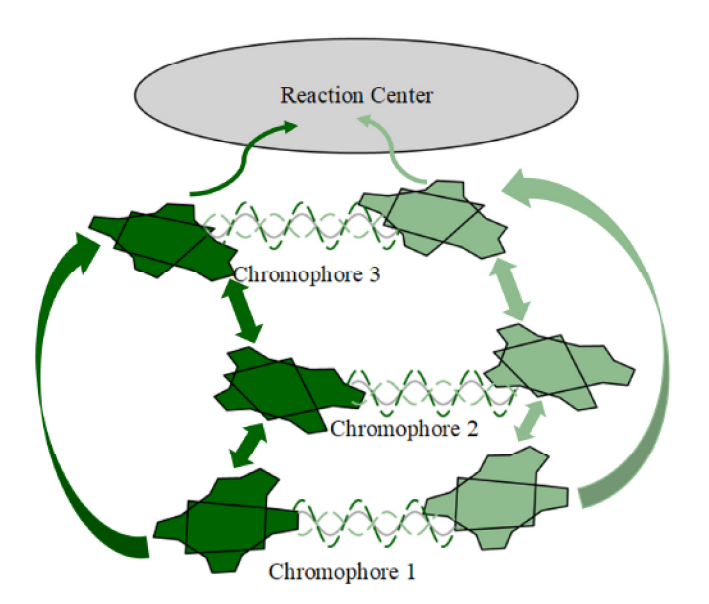


FIG. 1. Two pathways represented by the two sites of each chromophore. When  $\xi = 0$ , there is no cross-site interchromophore coupling, as shown. When V > 0, there is coupling, resulting in quantum interference between the sites of each chromophore. The waves demonstrate that the quantum interference can be either constructive or destructive, with constructive interference enhancing the energy-transfer efficiency.

intrachromophore coupling equal to the site energy scaled by a coupling parameter, V. This creates several equivalent interacting paths for exciton transfer to the reaction center and is represented pictorially for two sites per chromophore in Fig. 1. In the results presented here, we limit cross-site coupling to intrachromophore coupling and do not allow interchromophore cross-site coupling (e.g., site 1 on chromophore 1 is coupled to site 1 on chromophore 2, but not site 2 on chromophore 2); however, results for the model with interchromophore cross-site coupling are given in the Supplemental Material [48]. Additionally, Ref. [47] demonstrates that, due to quantum redundancy in the FMO complex, a subsystem of the first three chromophores transfers excitons to the reaction center more efficiently than the full seven chromophore system and is sufficient to characterize the dynamics of the FMO subcomplex. We therefore use this three chromophore subsystem and note that the general behavior of the dynamics is equivalent to using the full seven chromophore complex (see the Supplemental Material [48] for more details). We simulate the dynamics of exciton transfer by evolving the density matrix according to the quantum Liouville equation with a Lindblad operator, following Refs. [15,27,28,30,39,47]. The density matrix is constrained to allow only for single excitations, meaning that across the whole FMO complex (consisting of the chromophores and the reaction center) there is exactly one exciton. This is consistent with the idea that, in natural systems, photoexcitation events are sufficiently rare that multiexcitation states will not form [49]. Details of the model can be found in Sec. IV.

## A. Population dynamics

The one-body model serves as a reference to show the evolution of the dynamics in the absence of intrachromophore coupling. In Fig. 2(a), the population dynamics of the one-body model is shown in comparison to those of the coupled model with V = 0.6 and M = 20, where M is the number of sites per chromophore. The overall shape of the dynamics and frequencies of the oscillations are the same in both the one-body and coupled models. However, relative to the uncoupled model, the coupled model transfers greater exciton population to the reaction center within the same period of time and, consequently, the populations in chromophores 1 and 2 decay more rapidly. The degree to which the rate of transfer to the reaction center changes is influenced not only by the addition of more sites to the coupled model, but also by the magnitude of the intrachromophore coupling (V) and the initial excitation conditions. We examine combinations of these three possible factors to understand how each influences energy transfer and exciton condensation in the model.

There are two extreme limits of possible initial excitation conditions: an excitation entangled across all the sites of chromophore 1—referred to as the entangled excitation—and an excitation localized to a single site on chromophore 1—referred to as the localized excitation. The two initial excitation conditions represent subtly different models, in the sense that, by beginning from an entangled excitation, each site on chromophore 1 begins with identical populations, so the model has *M* identical interacting pathways for exciton transport, while localizing

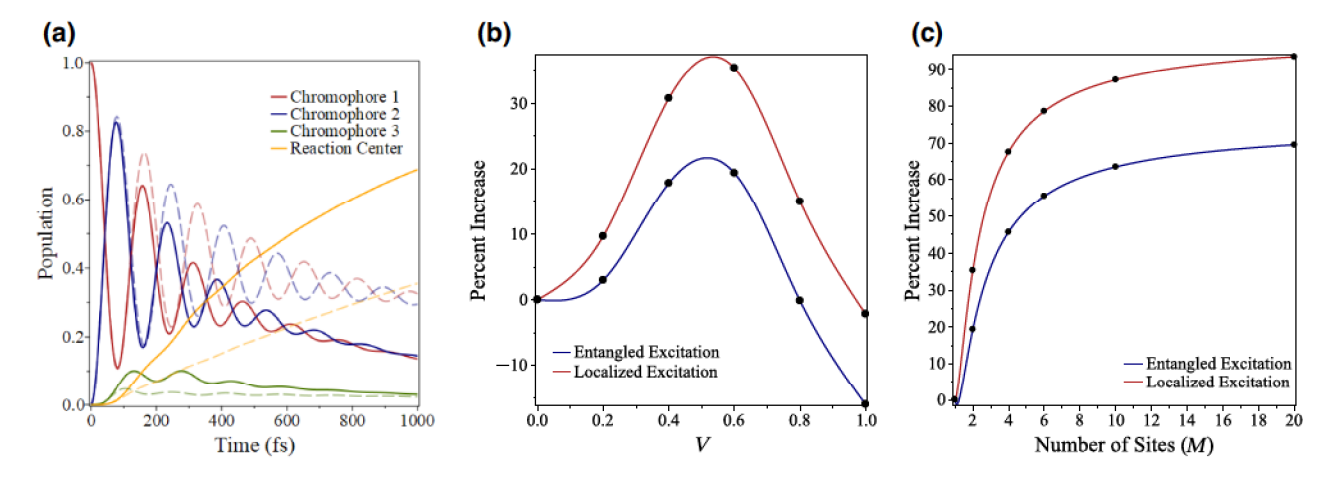


FIG. 2. (a) Population dynamics of the one-body model are shown as pale dashed lines, and population dynamics for the coupled model with V=0.6 and M=20 are shown as dark solid lines. (b) Percentage increase in population of the reaction center relative to the uncoupled model after 1000 fs for the entangled initial excitation model (blue) and localized initial excitation model (red) with two sites per chromophore for varying values of V. Increase in population reaches a maximum for V=0.6 at 42.5% for the entangled initial excitation and 48.2% for the localized initial excitation model, and a minimum for V=1 at -16.1% for the entangled initial excitation model and -2.2% for the localized site excitation model. (c) Percentage increase in population in the reaction center relative to the uncoupled model after 1000 fs as a function of M for the entangled initial excitation (blue) and localized excitation (red). Percentage increase is fitted to a third-order 1/M fit, which asymptotically approaches 75.5% for the entangled initial excitation and 99.4% for the localized initial excitation; fits are represented with solid lines.

the initial excitation on a single site distinguishes one site such that the *M* pathways are not necessarily identical. The entangled excitation represents a case with maximum possible intrachromophore entanglement, as all sites within the chromophores are equivalent, but the localized excitation is likely to be more physical, since the populations on all sites within a given chromophore are unlikely to be identical, particularly for a disordered material. We present results with both initial excitation conditions.

To explore the influence of intrachromophore coupling on the rate of exciton transfer to the reaction center, we vary the value of the parameter V from 0 to 1 in increments of 0.2 for the coupled model with M=2. Figure 2(b) shows a plot comparing the increase in the reaction center population relative to the uncoupled model after 1000 fs for the entangled and localized initial excitations. For both initial excitation conditions, intrachromophore coupling of V = 0.6 yields the greatest reaction center population, with enhancement of the reaction center population by 42.5% and 48.2% for the entangled and localized excitations, respectively. This indicates that greater intrachromophore coupling does not necessarily result in more efficient transfer of excitons to the reaction center. In fact, there are values of V that instead reduce the efficiency of transfer to the reaction center. Notably, when V = 1, the population of the reaction center is reduced relative to the uncoupled model by 16.2% for the entangled excitation and 2.2% for the localized excitation. The enhancement or reduction of the final reaction center population after 1000 fs corresponds to changes in the transfer rate over the course of the simulation. Plots of the rate of transfer of excitons to the reaction center are found in the Supplemental Material [48].

We hypothesize that the differences in the rates of transfer for different values of V are the result of quantum interference introduced by intrachromophore coupling. Increases in the rate of transfer result from constructive interference, whereas decreases result from destructive interference. This is supported by evidence of interference patterns in populations of different sites on the same chromophore for localized excitation; for more details, see the Supplemental Material [48]. For the model with interchromophore cross-site coupling allowed, or  $\xi > 0$ , the efficiency of exciton transfer to the reaction center is reduced, which we also attribute to destructive interference between sites and chromophores (see the Supplemental Material [48] for details). As we observe, the most efficient exciton transfer is for V = 0.6 and  $\xi = 0$ . We use these parameters for the remainder of the results presented here, unless otherwise specified, although some additional results are given in the Supplemental Material [48].

We examine the effect of the number of sites per chromophore on exciton transfer for M = 2, 4, 6, 10, and 20. Figure 2(c) shows plots of the increase in reaction center population relative to the uncoupled model after 1000 fs

for both the entangled and localized initial excitations. As can be seen from Fig. 2(c), for both initial excitation conditions, increasing the number of sites per chromophore enhances exciton transfer. The population of the reaction center after 1000 fs increases with M in an approximately 1/M manner, and when the data are fitted to first-, second-, and third-order 1/M models, the best fit is the third-order fit for either excitation condition. For the entangled initial excitation, the resulting third-order equation of fit is

% increase = 
$$75.5 - \frac{118.5}{M} - \frac{18.4}{M^2} + \frac{61.4}{M^3}$$
, (1)

demonstrating that, for the entangled excitation, the increase in the reaction center population relative to the uncoupled model asymptotically approaches a 75.5 enhancement. The corresponding fit for the localized excitation yields

% increase = 
$$99.4 - \frac{115.8}{M} - \frac{65.5}{M^2} + \frac{81.9}{M^3}$$
, (2)

showing that the increase in population asymptotically approaches 99.4% enhancement for the localized excitation. Therefore, we can conclude that the enhancement of transfer of excitons to the reaction center has a finite increase with the number of sites per chromophore and is greater with a localized initial excitation.

### B. Exciton condensation dynamics

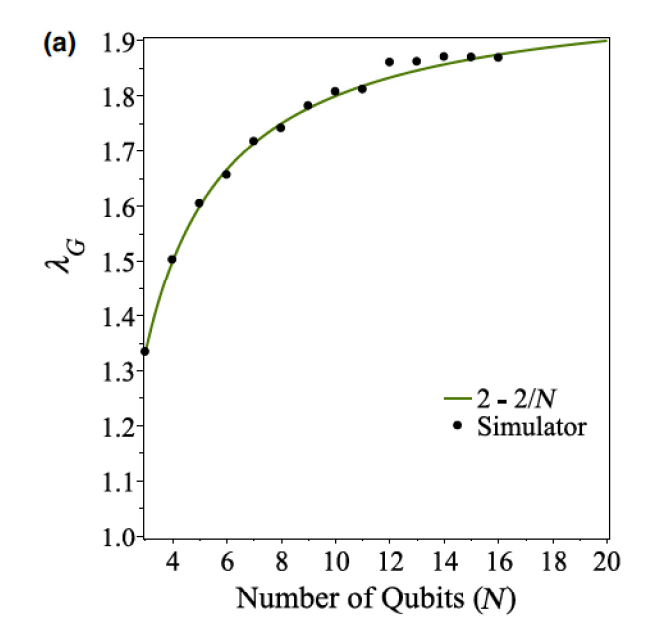
Exciton condensation occurs when excitons (particlehole pairs) become entangled and condense to occupy the same quantum state. The process results in long-range order-specifically off-diagonal long-range order-in the system and has a signature in the particle-hole reduced density matrix (RDM). In an uncorrelated system, the eigenvalues of the particle-hole RDM have a maximum bound of one. The entanglement associated with condensation and off-diagonal long-range order, however, produces an eigenvalue greater than one, the magnitude of which is indicative of the extent of long-range order or condensation. In the particle-hole RDM, one eigenvalue greater than one, corresponding to ground-state-to-ground-state projection, is always present, but a second large eigenvalue is a signature of exciton condensation [21,50,51]. The first large eigenvalue, which is extraneous with respect to exciton condensation, can be removed to create a modified particle-hole RDM, such that, in the modified RDM, any large eigenvalue is a signature of exciton condensation. We denote this large eigenvalue signature as  $\lambda_G$ . The density matrix of the FMO model represents a subblock of the modified particle-hole RDM, corresponding to possible single-excitation states, which we call the excitation matrix. However, because of the constraints on the model (i.e., only single-excitation states are possible), the signature of exciton condensation is constrained to exist within a second subblock of the modified particle-hole RDM, the *deexcitation* matrix, corresponding to the possible deexcited states in the single-excitation manifold. The excitation and deexcitation matrices are related by the single-excitation constraints, such that the deexcitation matrix can be obtained directly from the excitation matrix. We use this relationship to obtain the deexcitation matrix for the FMO model and probe the evolution of the signature of exciton condensation ( $\lambda_G$ ) over time.

In quantum computations, for a given number of qubits, the *W* state refers to a quantum superposition of all possible singly excited pure states, which is represented by

$$\frac{1}{\sqrt{N}}(|100\cdots0\rangle + |010\cdots0\rangle + \cdots + |000\cdots1\rangle), \quad (3)$$

where N is the number of qubits. If each qubit is taken to represent a particle-hole paired two-level system, where either the bottom level is occupied ( $|0\rangle$ ) or the top level is occupied ( $|1\rangle$ ), a system composed of N qubits can be viewed as two N-degenerate energy levels, each consisting of one fermion and two distinct orbitals. In this framework, then, the W state represents the maximal entanglement of a single-exciton system, with the theoretically predicted and computed values of  $\lambda_G$  being the maximum possible value for a certain number of entangled excitons within a single-excitation manifold. Figure 3(a) shows the signature of exciton condensation ( $\lambda_G$ ) for W-state systems with 3-16 qubits (i.e., 3-16 particles in 6-32 orbitals) prepared on IBM's QASM simulator, with  $\lambda_G$  being obtained from postmeasurement analysis, according to the procedure outlined in Ref. [22]. To obtain a large eigenvalue  $(\lambda_G > 1)$ , a minimum of three qubits are necessary, for which  $\lambda_G \approx 1.33$ . The magnitude of the large eigenvalue then grows with system size, according to 2 - 2/N. A derivation of the 2-2/N scaling for the large eigenvalue is given in Sec. IV.

In our model of chromophores, each qubit is analogous to a single site on a chromophore, such that, if all sites on a single chromophore are maximally entangled—as in the entangled initial excitation—this would form a state similar to a W state on that chromophore. Additionally, while states can be entangled in a nonmaximal way to produce a large eigenvalue, the expression 2 - 2/N is a maximum bound on the value of  $\lambda_G$  for a given number of entangled chromophore sites. As a minimum of three chromophore sites are necessary to form a condensed state, and all the exciton population is contained in a single chromophore at the initial time step, only the entangled initial excitation model with M = 4, 6, 10, and 20 can theoretically form a condensed state through intrachromophore entanglement. However, because there are three chromophores in the model, after the initial time step, all models can potentially form a condensed state through



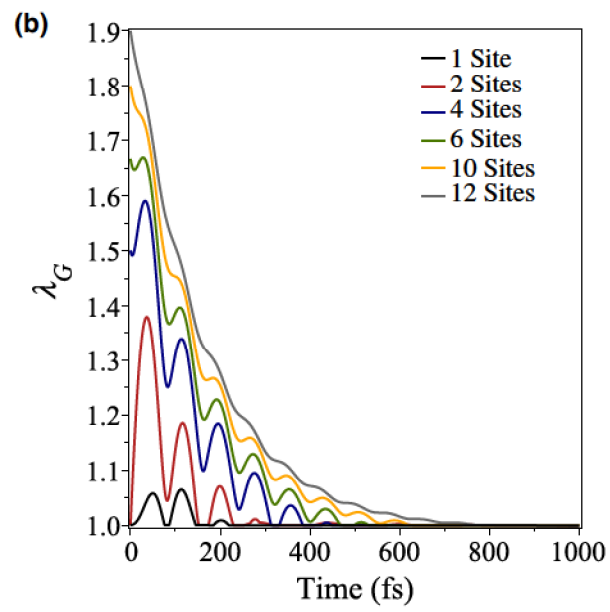
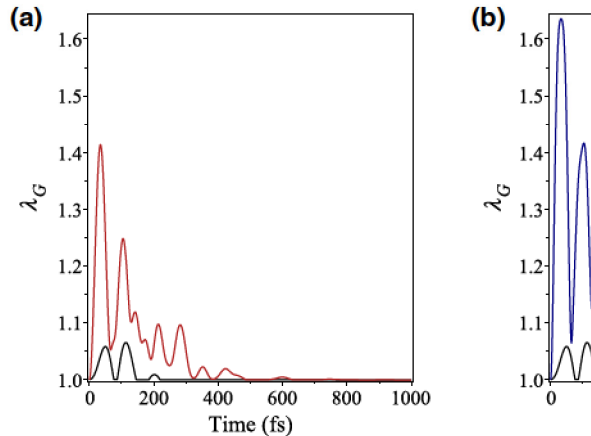
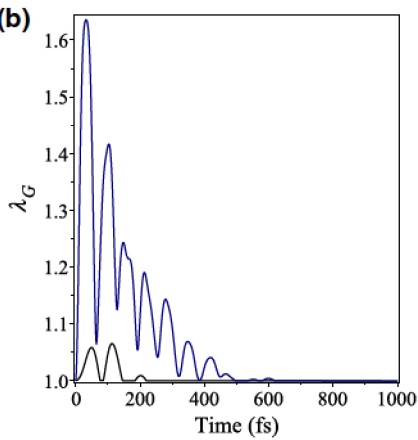


FIG. 3. (a) Maximum eigenvalues for maximally entangled stats of N qubits. (b)  $\lambda_G$  dynamics for M = 1, 2, 4, 6, 10, and 20 with entangled initial excitation.

interchromophore exciton entanglement or a combination of intra- and interchromophore exciton entanglement.

The dynamics of the entangled excitation model are consistent with the bound on  $\lambda_G$  for a maximally entangled state. Figure 3(b) shows that, for M > 2, the initial eigenvalue exactly matches the theoretically predicted value for the entanglement of the same number of qubits, e.g., for M = 20, initially  $\lambda_G = 1.9$ , and for 20 qubits, the predicted maximum is  $\lambda_G = 1.9$ . Notably, interchromophore exciton entanglement results in large eigenvalues, even in the uncoupled, M = 2, and localized excitation cases, where no condensation due to intrachromophore





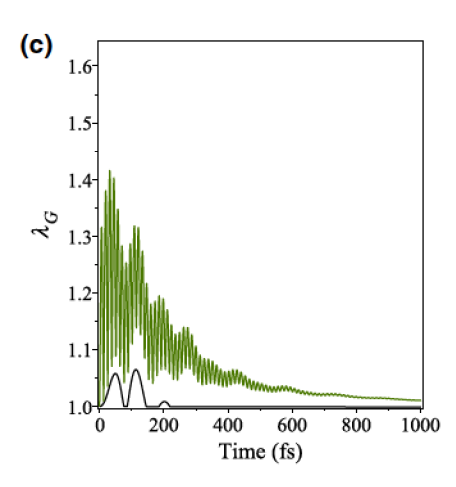


FIG. 4. Dynamics of  $\lambda_G$  for the single initial excitation model with V = 0.6 for (a) M = 2, (b) M = 4, and (c) M = 20.  $\lambda_G$  dynamics of the uncoupled model is shown in black on each plot.

entanglement is possible at the initial time step. Plots of the  $\lambda_G$  dynamics for M=2,4, and 20 with a localized initial excitation are shown in Fig. 4, and a summary of the maximum peak heights, number of peaks, and coherence times for all values of M are given in Table I (see the Supplemental Material [48] for additional plots). In the M=2 case, the large eigenvalue reaches a maximum around  $\lambda_G = 1.4$  for both entangled and localized excitations, which is larger than the theoretically predicted maximum for three entangled chromophores ( $\lambda_G \approx 1.33$ ) possible due to purely interchromophore coupling. Similarly, for M=4 and M=6, in the entangled excitation spectra, larger eigenvalue peaks appear in the spectra after the initial time step, and the maxima in the localized excitation spectra are of similar magnitude to these peaks. Interestingly, unlike the entangled excitation, where the value of M is clearly connected to the magnitude of the initial largest eigenvalue, for the localized excitation, the magnitude of the largest eigenvalue peak is independent of the number of sites. In fact, the largest eigenvalue is attained for M = 6, where the maximum is  $\lambda_G = 1.65$ , and the maximum eigenvalues are between 1.4 and 1.65 for all values of M. Consequently—except for the peaks in the initial time step of the entangled excitation—the large eigenvalues in the dynamics must result from a combination of intra- and interchromophore exciton entanglement.

For the entangled initial excitation, the frequency and peak positions in all the spectra are the same,

TABLE I. Spectral summary of the localized excitation model with M = 2, 4, 6, 10, and 20.

Number of sites	2	4	6	10	20
Maximum $\lambda_G$	1.41	1.64	1.65	1.56	1.42
Number of peaks	8	8	15	40	79
Coherence time (fs)	463	483	634	1000	1000

independent of the number of sites or the magnitude of the peaks—although for M = 10 and M = 20 the peaks are small compared to the initially large magnitude of  $\lambda_G$ . However, for the localized excitation, the frequency and coherence time increase with the number of sites. While for M = 2, 4, and 6, the value of  $\lambda_G$  decays to one near 463, 483, and 634 fs, respectively; for M = 10 and M = 20, the value of  $\lambda_G$  is greater than one at 1000 fs, and we observe fast narrow peaks in the M = 20 spectrum in Fig. 4(c). This suggests that the evolution of  $\lambda_G$  in both the entangled and localized excitations is due to an interchromophore mechanism inherent to the exciton dynamics, although the individual peaks in  $\lambda_G$  result from a combination of interand intrachromophore coupling. By analyzing the populations of the chromophores for the large eigenvalue mode (see the Supplemental Material [48] for details), we see that major peaks occur where the populations of chromophores 1 and 2 are nearly equal. As a result, the peaks follow approximately the same pattern as the oscillation of the exciton transfer between chromophores 1 and 2. Additionally, in the entangled excitation, all sites have identical populations, such that both inter- and intrachromophore exciton entanglement play a role in the large eigenvalue. Even for the localized excitation, although not all sites on each chromophore have identical populations, the largest peaks often occur where the populations of several sites are similar. The intrachromophore interactions due to nonidentical site populations are likely the cause of the increased peak frequency in the localized excitation spectra. However, for both entangled and localized excitations, the main dynamics appear to result from a combination of intraand interchromophore coupling between chromophores 1 and 2.

One notable feature of the  $\lambda_G$  dynamics is the decay of the large eigenvalue. In all cases, the maximum value of  $\lambda_G$  is reached within the first 100 fs, after which the eigenvalue gradually decays towards one and has almost

completely decayed by the region of 400-600 fs. Even in the localized models for M = 10 and M = 20, which show coherence over the full 1000 fs simulation, the eigenvalue is only marginally greater than one after about 500 fs. Interestingly, we note that in this region the rate of transfer to the reaction center also declines (see the Supplemental Material [48] for more details). Moreover, when dephasing is eliminated—resulting in a majority of the exciton population remaining trapped between chromophores 1 and 2-the decay of the large eigenvalue is reduced. In fact, as the populations reach a steady state, with the majority of the population oscillating between chromophores 1 and 2, the large eigenvalue also reaches a steady state with a magnitude markedly greater than one. (Plots showing these results are found in the Supplemental Material [48].) This is consistent with the fact that chromophores 1 and 2 have the greatest populations in the large eigenvalue and suggests that the large eigenvalue results primarily from entanglement of these two chromophores.

The results presented here utilize a coupling parameter of V = 0.6; however, the trends are applicable to varying

values of V. For the entangled excitation case, the  $\lambda_G$ dynamics are relatively invariant to the value of V. For the localized excitation, for various V > 0, while some variation exists in the maximum value of  $\lambda_G$ , we still observe large eigenvalues and spectral shapes similar to those shown in Fig. 4. Plots of these results are provided in the Supplemental Material [48]. As with large values of M, larger values of V increase the peak frequency of  $\lambda_G$ , which likely results from increased intrachromophore interactions caused by greater coupling between sites on the same chromophores. We also observe that, as long as the intrachromophore interaction is nonzero, the introduction of interchromophore (cross-site) coupling, while reducing the overall exciton transfer efficiency, changes neither the large eigenvalue nor the general features of the dynamics (see the Supplemental Material [48] for more details).

To understand how excitons are transferred by the mode associated with the large eigenvalue versus the other eigenvalues, we examine the breakdown of the total deexcitation population into populations associated with the individual

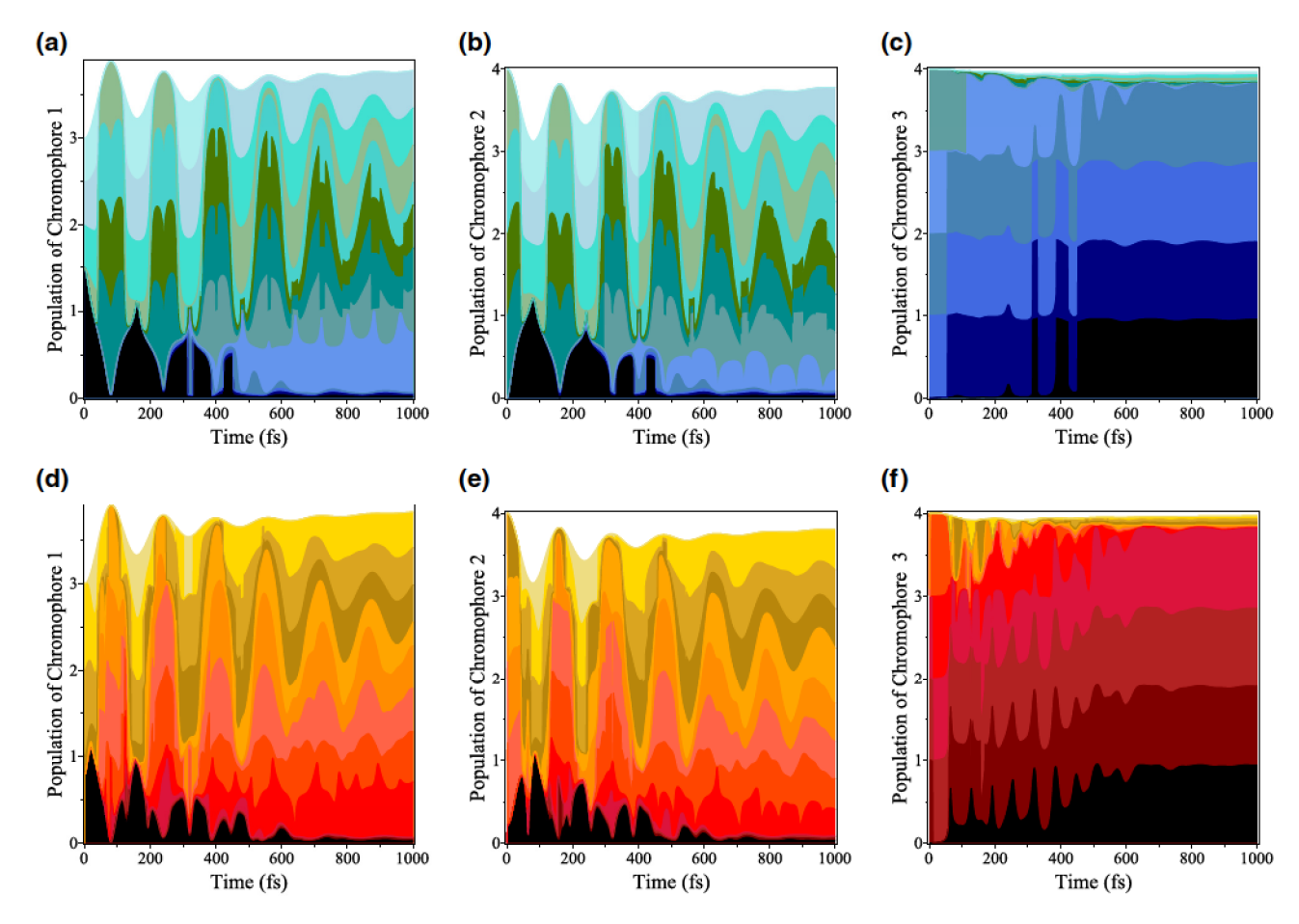


FIG. 5. Breakdown of the deexcitation populations for chromophores 1 (a), 2 (b), and 3 (c) for the entangled initial excitation and populations of the modes for chromophores 1 (d), 2 (e), and 3 (f) for the localized initial excitation with V = 0.6 and M = 4. Lowest curve in the darkest shade represents the populations associated with the large eigenvalue mode, with each successive layer adding the populations from the next largest eigenvalue. Populations from each mode sum to the total deexcitation populations.

eigenvalues of the deexcitation matrix. Figure 5 shows the breakdown of the populations for each chromophore for both entangled and localized excitations with M=4. The lowest level in the plots shows the populations of the large eigenvalue, and each successive level adds the populations from the next largest eigenvalue. Both excitation conditions show similar trends in the dynamics of the deexcitation populations of the large eigenvalue. Interestingly, for chromophores 1 and 2, the populations of the large eigenvalue oscillate with the same frequency as the total populations, until the eigenvalue decays (around 500 fs). However, the populations of the large eigenvalue are out of phase with the total deexcitation populations, while all other eigenvalues with significant populations are in phase with the total populations. This is notable because the population of the large eigenvalue is in phase with the excitation population transfer rather than the deexcitation population transfer.

For chromophore 3, the population in the large eigenvalue is relatively small until the large eigenvalue decays, at which point the population increases significantly. This is consistent with the idea that the large eigenvalue primarily results from entanglement between sites on chromophores 1 and 2 decaying as the population is passed to the reaction center and supports the hypothesis that the entanglement associated with the large eigenvalue helps to facilitate transfer of excitons between chromophores 1 and 2. The deexcitation populations of chromophore 3 are also proportional to the rate of transfer of deexcitation population to the reaction center, which is the inverse of the rate of exciton transfer to the reaction center. Therefore, we observe a decrease in exciton transfer from the large eigenvalue (indicated by an increase in deexcitation transfer) after the decay of the large eigenvalue. This behavior is unique to this eigenvalue, as other eigenvalues either have little contribution to the total rate of deexcitation transfer or do not exhibit an increase in deexcitation transfer.

### III. CONCLUSIONS

Our results reveal the potential for enhanced energy transfer in photosynthetic light-harvesting complexes through a microscopic exciton-condensation-like mechanism. We show that in the correlated model of the FMO complex there is a large eigenvalue signature of exciton condensation that evolves with the population transfer dynamics. In the single-excitation manifold, exciton condensation in the macroscopic sense is not possible; however, the signature we observe indicates the beginnings of long-range order associated with local condensation or entanglement of excitons, which leads to macroscopic condensation in larger systems. Local condensation of this type is consistent with the perspective of collective phenomena that form emergent condensate states [52,53], and in the single-excitation manifold, there is a microscopic

case of the emergent phenomenon. Thus, while in small systems like light-harvesting complexes the exciton entanglement indicated by the large eigenvalue may lack some of the properties associated with macroscopic exciton condensation, it is likely to retain many of the advantages, including efficient energy transfer. This is evident in our results, where—with the appropriate tuning of model parameters, including the number of sites per chromophore and intrachromophore coupling—we show that exciton transfer can be enhanced by nearly 100% relative to a onebody model through the limited exciton-condensation-like mechanism. Moreover, even under conditions where the model parameters are less than ideally tuned, the excitoncondensate-like mechanism and enhancement of exciton transfer are still possible. Although this mechanism does not appear to inherently increase exciton transport, in a carefully tuned system, it creates the potential for significant amplification of energy transfer.

Because amplification of energy transfer through an exciton-condensation-like mechanism is possible in a noisy room-temperature process like photosynthesis, such a mechanism can potentially be harnessed to enhance energy transfer in other similar systems or conditions. The parameters of the model represent meaningful properties with relevance to physical systems. The intrachromophore coupling is comparable to  $\pi$ - $\pi$  interactions within molecules, like the porphyrin ring chromophores in FMO. The beginnings of exciton condensation have been computed in van der Waals stacks of benzene and finite analogs of the graphene bilayer [23,24]. The large range of values of intrachromophore coupling over which we observe the exciton-condensate-like mechanism in the FMO model suggests a broad range of appropriate couplings for which real materials may exhibit an exciton-condensate-like mechanism. Furthermore, when coupling is allowed between nonidentical sites on different chromophores, the exciton-condensate-like mechanism still occurs; this has important implications for the possibility of the mechanism in disordered materials. Although the model resembles an ideal case of a light-harvesting complex, the robustness of the excitoncondensate-like mechanism to variations in the coupling parameters suggests its potential applicability to the optimization of real materials with respect to energy transfer efficiency.

By linking exciton condensation to the transfer of energy in light-harvesting complexes, we observe a pattern for understanding the principles of efficient energy transfer. These principles can be applied to designing synthetic materials that utilize the same type of limited exciton-condensation-like mechanism. Whereas the vision of superfluid energy transfer through macroscopic exciton condensation remains difficult to realize under reasonable conditions, the mechanism of limited exciton condensation may be used to develop materials that are able to transfer

energy with extremely high efficiency under conditions conducive to wide applicability.

### IV. METHODS

## A. Signature of exciton condensation

Exciton condensation results from entanglement of particle-hole pairs (excitons). The entanglement of excitons is exhibited as long-range order—specifically, off-diagonal long-range order—in the particle-hole RDM:

$${}^{2}G_{k,l}^{i,j} = \langle \psi | \hat{a}_{i}^{\dagger} \hat{a}_{j} \hat{a}_{l}^{\dagger} \hat{a}_{k} | \psi \rangle, \tag{4}$$

where  $\hat{a}_i^{\dagger}$  and  $\hat{a}_j$  are fermion creation and annihilation operators, and  $|\psi\rangle$  is the wave function. In an uncorrelated fermion density matrix, like the particle-hole RDM, the eigenvalues of the matrix are bound by a maximum value of one. However, in a highly correlated system, such as one exhibiting exciton condensation, the associated longrange order results in a large eigenvalue (greater than one). A large eigenvalue in the particle-hole RDM is therefore a signature of exciton condensation, and the magnitude of the eigenvalue describes the extent of condensation, as it corresponds to the occupation of the condensed state [21,50,51].

Even in the absence of correlation, the particle-hole RDM always contains one large eigenvalue, corresponding to ground-state-to-ground-state projection, that is extraneous with respect to exciton condensation. The first large eigenvalue of the particle-hole RDM, not related to exciton condensation, can be removed from the particle-hole RDM using a modified particle-hole RDM,  ${}^2\tilde{G}_{kJ}^{i,j}$ :

$${}^{2}\tilde{G}_{k,l}^{i,j} = {}^{2}G_{k,l}^{i,j} - {}^{1}D_{j}^{i}{}^{1}D_{k}^{l}, \tag{5}$$

where  ${}^{1}D_{j}^{i}$  is the one-particle RDM. Once the extraneous large eigenvalue is removed, any eigenvalue greater than one in the modified particle-hole matrix is a signature for exciton condensation. The eigenvalues of the modified particle-hole RDM are calculated as

$$^{2}\tilde{G}v_{i}=\lambda_{i}v_{i}. \tag{6}$$

We use the large eigenvalue signature of the particle-hole RDM to characterize exciton condensation in a model system of the light-harvesting complex and make connections to energy transfer.

#### B. FMO model

We define the FMO complex through its density matrices, its model Hamiltonian, and its environmental channels in Secs. IV B 2, IV B 1, and IV B 3, respectively. In particular, we show that, when the dynamics is restricted to the single-excitation manifold, the particle-hole reduced

density matrix,  ${}^2G$ , has an excitation subblock and a deexcitation subblock, with any potential exciton condensation occurring within the deexcitation subblock. Moreover, we generalize the FMO model to support multiple sites on each chromophore, the correlation of which can be controlled to enhance transport.

### 1. Model Hamiltonian

Exciton transfer in the FMO complex has been the subject of extensive theoretical study using model Hamiltonians [27–29,39,40,47], specifically, the one-body Hamiltonian:

$$\hat{H} = \frac{1}{2} \sum_{s,m} m \epsilon_s \hat{a}_{s,m}^{\dagger} \hat{a}_{s,m} + \sum_{s \neq t} U_{s,t} \hat{a}_{s,+1}^{\dagger} \hat{a}_{s,-1} \hat{a}_{t,-1}^{\dagger} \hat{a}_{t,+1}, \quad (7)$$

which models each exciton as a single-electron excitation. In the Hamiltonian, s and t represent the sites of the chromophores, m is the energy level (either +1 or -1) within the chromophore, and  $\hat{a}_{s,m}^{\dagger}$  ( $\hat{a}_{s,m}$ ) creates (annihilates) an electron of energy level m on site s. The one-body Hamiltonian is so called because it contains only one-body interactions. While this one-body Hamiltonian accurately captures the transport of excitons in the FMO complex, it fails to account for strong correlation between electrons on the same chromophore. Prior research accounts for this by using a Lipkin model [30] or adding coupling terms [31,32], which can introduce additional sites on the individual chromophores to help account for this correlation. We develop a coupled model Hamiltonian to explicitly introduce strong electron correlation by expanding the onebody model to have additional sites on each chromophore and include intra- and interchromophore coupling terms. The Hamiltonian for this model is defined as

$$\hat{H} = \frac{1}{2} \sum_{s,m,p} m \epsilon_s \hat{a}^{\dagger}_{s,m,p} \hat{a}_{s,m,p}$$

$$+ (1 - \xi) \sum_{s \neq t,p} U_{s,t} \hat{a}^{\dagger}_{s,+1,p} \hat{a}_{s,-1,p} \hat{a}^{\dagger}_{t,-1,p} \hat{a}_{t,+1,p}$$

$$+ \frac{1}{2} V \sum_{s,m,p,q} \epsilon_s \hat{a}^{\dagger}_{s,m,p} \hat{a}^{\dagger}_{s,-m,q} \hat{a}_{s,m,q} \hat{a}_{s,-m,p}$$

$$+ \xi \sum_{s \neq t,p \neq q} U_{s,t} \hat{a}^{\dagger}_{s,+1,p} \hat{a}_{s,-1,p} \hat{a}^{\dagger}_{t,-1,q} \hat{a}_{t,+1,q}, \qquad (8)$$

where, following the one-body Hamiltonian, s and t are chromophore sites, p and q represent the sites within the chromophore, and m is the energy level. The V term represents coupling between sites on the same chromophore and  $\xi$  represents coupling between sites on different chromophores. The one-body Hamiltonian site energy and interchromophore coupling values are obtained from the  $7 \times 7$  Hamiltonian of Ref. [27].

The addition of sites to the chromophores creates multiple paths for exciton transfer. When V=0 and  $\xi=0$ , the paths are completely isolated, and excitons cannot be transferred between the paths. In essence, this results in M (where M is the number of sites per chromophore) onebody models, which can only transfer through multiple paths if the initial excited state is entangled between all sites on the same chromophore. For this case, all the paths would transfer equivalent fractions of the population proportional to 1/M. If the initial excitation were localized to a single site, exciton population would instead be constrained to a single pathway and function identically to the one-body model. When V > 0, there is intrachromophore coupling between the pathways, scaled by the value of V. This results in transfer of exciton population between pathways via intrachromophore population exchange, even in the case where the initial excitation is localized to a single site on a single chromophore. In Fig. 1, intrachromophore coupling is represented as wave patterns between different sites of the same chromophore, indicating that either constructive and destructive interference can result from such coupling. For values of  $\xi = 0$ , the transfer of exciton population between chromophores is isolated such that each site on a specified chromophore can only transfer to the corresponding site on the other chromophores, i.e., site 1 on chromophore 1 is only coupled to site 1 on chromophores 2 and 3, and site 2 on chromophore 1 is coupled to site 2 on chromophores 2 and 3, thus allowing interchromophore coupling only within, but not between, pathways. When  $\xi > 0$ , exchange of population between chromophores is balanced by the  $\xi$  and  $1 - \xi$  terms of the Hamiltonian to also allow transfer between the paths via interchromophore cross-site coupling, i.e., site 1 on chromophore 1 is coupled to all sites on chromophores 2 and 3. We find that, for values of  $\xi > 0$ , transfer of excitons to the reaction center is much less efficient, because interchromophore cross-site coupling between pathways opens additional channels for destructive interference, which reduces the overall exciton transfer in the model. Consequently, we focus on the coupled model with  $\xi = 0$ . However, we observe a large eigenvalue in all cases where there is potential for interaction between sites on a chromophore (e.g., entangled starting excitation or  $\xi \neq 0$  or 1). Results for both population and  $\lambda_G$  dynamics with  $\xi \neq 0$  are given in the Supplemental Material [48].

Although we express Eqs. (7) and (8) in the electron basis, which represents each chromophore as an electron in a two-level orbital, where an exciton is created by excitation of an electron from the lower level of the orbital to the upper level, both Hamiltonians can be equivalently expressed in an exciton basis, where each chromophore or chromophore site is represented by a single orbital of a specific energy that may be occupied by an exciton. A pictorial representation demonstrating the two equivalent bases is given in the Supplemental Material [48].

We also constrain our model to allow only for single excitations.

### 2. Density matrices

The FMO complex consists of three subcomplexes, each consisting of seven (or eight) chromophores [44,46], which transfer energy in the form of excitons to a reaction center. The properties of the FMO complex can be modeled for a single subcomplex in an exciton basis by representing each chromophore as a one-level orbital, which is either empty or occupied by an exciton. An  $N \times N$  density matrix (where N is the number of chromophores multiplied by M) representing this system can be described by

$$D = \langle \psi | \hat{\sigma}_s^{\dagger} \hat{\sigma}_s | \psi \rangle, \tag{9}$$

where  $\hat{\sigma}_s^{\dagger}$  ( $\hat{\sigma}_s$ ) is the creation (annihilation) operator of one exciton on chromophore s, and  $\psi$  is the wave function of the FMO model system. This can also be equivalently expressed in the electron basis. In the electron basis, the density matrix is

$$D = \langle \psi | \hat{a}_{s-1}^{\dagger} \hat{a}_{s,+1} \hat{a}_{s+1}^{\dagger} \hat{a}_{s,-1} | \psi \rangle, \tag{10}$$

where  $\hat{a}_{s,-1}^{\dagger}$  ( $\hat{a}_{s,-1}$ ) creates (destroys) an electron in the lower level of chromophore s, and  $\hat{a}_{s,+1}^{\dagger}$  ( $\hat{a}_{s,+1}$ ) creates (destroys) an electron in the upper level of chromophore s.

Using the electron basis, we can easily connect the exciton density matrix to the particle-hole RDM, which is a two-body matrix. Due to the equivalency of the exciton and electron bases, the density matrix, D, is a subblock of the modified particle-hole RDM [Eq. (5)], specifically an  $N \times N$  subblock of the *excited* states possible in the single-excitation manifold; we therefore refer to D as the excitation density matrix. Because our model allows only for single excitations, there is a constraint on the modified particle-hole density matrix that restricts the long-range order corresponding to exciton condensation existing entirely within a second  $N \times N$  subblock of the modified particle-hole matrix. This  $N \times N$  subblock corresponds to the possible deexcited states; we therefore refer to this as the deexcitation density matrix, G. The deexcitation density matrix is written as follows:

$$G = \langle \psi | \hat{a}_{s,\perp}^{\dagger} \hat{a}_{s,-1} \hat{a}_{s,-1}^{\dagger} \hat{a}_{s,+1}^{\dagger} | \psi \rangle. \tag{11}$$

If the modified particle-hole RDM has a large eigenvalue, the deexcitation density matrix has an identical large eigenvalue, signifying the long-range order associated with exciton condensation. This allows us to bypass calculation of the complete modified particle-hole matrix and instead calculate only the excitation and deexcitation

density matrices. The excitation and deexcitation density matrices are related by

$$G_{i,j} = \begin{cases} 1 - D_{i,j} & \text{for } i = j, \\ D_{i,j} & \text{for } i \neq j, \end{cases}$$
 (12)

where i and j are the indices of the matrix. Conceptually, this relationship indicates that the populations of the excited and deexcited electrons in a specific chromophore must sum to one, but the coupling between chromophores is equivalent whether in the excitation or deexcitation representation. This means that the excitation matrix has a trace of 1—because only a single excitation is allowed—while the deexcitation matrix has a trace of N-1. The relationship makes it possible to obtain the deexcitation density matrix directly from the calculated excitation density matrix.

## 3. Dynamics and environmental effects

The environmental effects and dynamics of exciton transport are calculated using the quantum Liouville equation with a Lindblad operator:

$$\frac{d}{dt}D = -\frac{i}{\hbar}[\hat{H}, D] + \hat{L}(D), \tag{13}$$

where D is the excitation density matrix, and Eq. (13) models the behavior of the density matrix over time. The Lindblad operator,  $\hat{L}(D)$ , is defined to account for dephasing, dissipation, and transfer to the reaction center (RC) as follows:

$$\hat{L}(D) = \hat{L}_{deph}(D) + \hat{L}_{diss}(D) + \hat{L}_{RC}(D),$$
 (14)

with

$$\hat{L}_{\text{deph}}(D) = \alpha \sum_{k} 2\langle k|D|k\rangle |k\rangle \langle k| - \{|k\rangle \langle k|, D\}, \qquad (15)$$

$$\hat{L}_{\text{diss}}(D) = \beta \sum_{k} 2\langle k|D|k\rangle|g\rangle\langle g| - \{|k\rangle\langle k|, D\}, \qquad (16)$$

$$\hat{L}_{RC}(D) = 2\gamma \sum_{\omega} \langle \omega | D | \omega \rangle | s \rangle \langle s | - \gamma \{ | \omega \rangle \langle \omega |, D \}, \quad (17)$$

where  $|g\rangle$  is the ground state of the Hamiltonian,  $|k\rangle$  is the excited state,  $|s\rangle$  is the reaction center, and  $|\omega\rangle$  is the first excited state of the specified site of chromophore 3.  $\alpha$ ,  $\beta$ , and  $\gamma$  are rate parameters chosen to be  $1.52 \times 10^{-4}$ ,  $7.26 \times 10^{-5}$ , and  $1.21 \times 10^{-8}$  atomic units, respectively. The Lindblad operator and the values of the parameters follow previous studies with both one-body [27] and correlated [30] models.

## C. Derivation of largest eigenvalue $\lambda_G^*$ for W state

Consider the expectation value of the particle-hole RDM:

$$\lambda_G = \sum_{i,j,k,l} g_{i,j} \left( {}^2 G_{k,l}^{i,j} \right) g_{k,l}^*, \tag{18}$$

$$= \sum_{i,j,k,l} g_{i,j} \langle \Psi | \hat{a}_i^{\dagger} \hat{a}_j \hat{a}_l^{\dagger} \hat{a}_k | \Psi \rangle g_{k,l}^*, \tag{19}$$

$$= \langle \Psi | \hat{g} \hat{g}^{\dagger} | \Psi \rangle, \tag{20}$$

where

$$\hat{g} = \sum_{ij} g_{ij} \hat{a}_i^{\dagger} \hat{a}_j. \tag{21}$$

Let the wave function be the W state of N qubits:

$$|\Psi\rangle = \frac{1}{\sqrt{N}} \left( |100 \cdots 0\rangle + |010 \cdots 0\rangle + \ldots \right). \tag{22}$$

The eigenvalue of the particle-hole RDM is maximized by selecting the eigenoperator  $\hat{g}^{\dagger}$  to represent a phase-coherent superposition of all single-particle excitations to maximize constructive interference:

$$\hat{g}^{\dagger} = \frac{1}{\sqrt{N}} \sum_{s=1}^{N} \hat{a}_{s,1}^{\dagger} \hat{a}_{s,0}, \tag{23}$$

where  $a_{s,0}^{\dagger}$  ( $a_{s,1}$ ) creates (destroys) a particle in the lower (upper) level of qubit s. The expectation values of the individual elements are

$$\langle \Psi | \hat{a}_{s,0}^{\dagger} \hat{a}_{s,1} \hat{a}_{t,1}^{\dagger} \hat{a}_{t,0} | \Psi \rangle = \begin{cases} \frac{N-1}{N} & \text{if } s = t, \\ \frac{1}{N} & \text{if } s \neq t. \end{cases}$$
(24)

Therefore, the maximum eigenvalue  $\lambda_G^*$  of the W state is

$$\lambda_{G}^{*} = \frac{1}{N} \langle \Psi | \sum_{s,t=1}^{N} \hat{a}_{s,0}^{\dagger} \hat{a}_{s,1} \hat{a}_{t,1}^{\dagger} \hat{a}_{t,0} | \Psi \rangle, \tag{25}$$

$$= \frac{1}{N} \left[ N \left( \frac{N-1}{N} \right) + N(N-1) \left( \frac{1}{N} \right) \right], \quad (26)$$

$$=2-\frac{2}{N}. (27)$$

In the limit that N approaches infinity, the largest eigenvalue is 2.

Data will be made available upon reasonable request. Code will be made available on a public Github repository upon publication.

### ACKNOWLEDGMENTS

D.A.M. gratefully acknowledges the U.S. National Science Foundation (Grant No. CHE-2155082), the NSF QuBBE Quantum Leap Challenge Institute (Grant No. NSF OMA-2121044), and the Department of Energy, Office of Basic Energy Sciences (Grant No. DE-SC0019215).

D.A.M. conceived of the project. A.O.S. and D.A.M. wrote the computational code. A.O.S. performed the calculations. A.O.S., L.M.S., and D.A.M. analyzed the data and wrote the manuscript.

The authors declare no competing interests.

- F. London, On the Bose-Einstein condensation, Phys. Rev. 54, 947 (1938).
- [2] J. M. Blatt, K. W. Böer, and W. Brandt, Bose-Einstein condensation of excitons, Phys. Rev. 126, 1691 (1962).
- [3] M. S. Fuhrer and A. R. Hamilton, Chasing the exciton condensate, Physics 9, 80 (2016).
- [4] P. B. Littlewood, P. R. Eastham, J. M. J. Keeling, F. M. Marchetti, B. D. Simons, and M. H. Szymanska, Models of coherent exciton condensation, J. Phys.: Condens. Matter 16, S3597 (2004).
- [5] D. V. Fil and S. I. Shevchenko, Electron-hole superconductivity (review), Low Temp. Phys. 44, 867 (2018).
- [6] L. V. Keldysh, Coherent states of excitons, Phys.-Usp. 60, 1180 (2017).
- [7] L. V. Butov, A. Zrenner, G. Abstreiter, G. Böhm, and G. Weimann, Condensation of Indirect Excitons in Coupled AlAs/GaAs Quantum Wells, Phys. Rev. Lett. 73, 304 (1994).
- [8] L. V. Butov, Exciton condensation in coupled quantum wells, Solid State Commun. 127, 89 (2003).
- [9] J. P. Eisenstein and A. H. MacDonald, Bose-Einstein condensation of excitons in bilayer electron systems, Nature 432, 691 (2004).
- [10] J. P. Eisenstein, Exciton condensation in bilayer quantum Hall systems, Annu. Rev. Condens. Matter Phys. 5, 159 (2014).
- [11] J. I. A. Li, T. Taniguchi, K. Watanabe, J. Hone, and C. R. Dean, Excitonic superfluid phase in double bilayer graphene, Nat. Phys. 13, 751 (2017).
- [12] X. Liu, K. Watanabe, T. Taniguchi, B. I. Halperin, and P. Kim, Quantum Hall drag of exciton condensate in graphene, Nat. Phys. 13, 746 (2017).
- [13] H. Min, R. Bistritzer, J.-J. Su, and A. H. MacDonald, Room-temperature superfluidity in graphene bilayers, Phys. Rev. B 78, 121401 (2008).
- [14] L. Sigl, F. Sigger, F. Kronowetter, J. Kiemle, J. Klein, K. Watanabe, T. Taniguchi, J. J. Finley, U. Wurstbauer, and A. W. Holleitner, Signatures of a degenerate many-body state of interlayer excitons in a van der Waals heterostack, Phys. Rev. Res. 2, 042044 (2020).
- [15] M. M. Fogler, L. V. Butov, and K. S. Novoselov, Hightemperature superfluidity with indirect excitons in van der Waals heterostructures, Nat. Commun. 5, 4555 (2014).

- [16] S. Gupta, A. Kutana, and B. I. Yakobson, Heterobilayers of 2D materials as a platform for excitonic superfluidity, Nat. Commun. 11, 2989 (2020).
- [17] A. Kogar, M. S. Rak, S. Vig, A. A. Husain, F. Flicker, Y. I. Joe, L. Venema, G. J. MacDougall, T. C. Chiang, E. Fradkin, J. van Wezel, and P. Abbamonte, Signatures of exciton condensation in a transition metal dichalcogenide, Science 358, 1314 (2017).
- [18] L. Ma, P. X. Nguyen, Z. Wang, Y. Zeng, K. Watanabe, T. Taniguchi, A. H. MacDonald, K. F. Mak, and J. Shan, Strongly correlated excitonic insulator in atomic double layers, Nature 598, 585 (2021).
- [19] J.-J. Su and A. H. MacDonald, Spatially indirect exciton condensate phases in double bilayer graphene, Phys. Rev. B 95, 045416 (2017).
- [20] M. Sun, A. V. Parafilo, K. H. A. Villegas, V. M. Kovalev, and I. G. Savenko, Bose-Einstein condensate-mediated superconductivity in graphene, 2D Mater. 8, 031004 (2021).
- [21] S. Safaei and D. A. Mazziotti, Quantum signature of exciton condensation, Phys. Rev. B 98, 045122 (2018).
- [22] L. M. Sager, S. E. Smart, and D. A. Mazziotti, Preparation of an exciton condensate of photons on a 53-qubit quantum computer, Phys. Rev. Res. 2, 043205 (2020).
- [23] A. O. Schouten, L. M. Sager, and D. A. Mazziotti, Exciton condensation in molecular-scale van der Waals stacks, J. Phys. Chem. Lett. 12, 9906 (2021).
- [24] L. M. Sager, A. O. Schouten, and D. A. Mazziotti, Beginnings of exciton condensation in coronene analog of graphene double layer, J. Chem. Phys. 156, 154702 (2022).
- [25] L. M. Sager and D. A. Mazziotti, Entangled phase of simultaneous fermion and exciton condensations realized, Phys. Rev. B 105, L121105 (2022).
- [26] J. Adolphs and T. Renger, How proteins trigger excitation energy transfer in the FMO complex of green sulfur bacteria, Biophys. J. 91, 2778 (2006).
- [27] M. B. Plenio and S. F. Huelga, Dephasing-assisted transport: Quantum networks and biomolecules, New J. Phys. 10, 113019 (2008).
- [28] F. Caruso, A. W. Chin, A. Datta, S. F. Huelga, and M. B. Plenio, Highly efficient energy excitation transfer in light-harvesting complexes: The fundamental role of noise-assisted transport, J. Chem. Phys. 131, 105106 (2009).
- [29] C. C. Forgy and D. A. Mazziotti, Relations between environmental noise and electronic coupling for optimal exciton transfer in one- and two-dimensional homogeneous and inhomogeneous quantum systems, J. Chem. Phys. 141, 224111 (2014).
- [30] D. A. Mazziotti, Effect of strong electron correlation on the efficiency of photosynthetic light harvesting, J. Chem. Phys. 137, 074117 (2012).
- [31] A. Mattioni, F. Caycedo-Soler, S. F. Huelga, and M. B. Plenio, Design Principles for Long-Range Energy Transfer at Room Temperature, Phys. Rev. X 11, 041003 (2021).
- [32] S. Davidson, F. A. Pollock, and E. Gauger, Eliminating Radiative Losses in Long-Range Exciton Transport, PRX Quantum 3, 020354 (2022).
- [33] G. S. Engel, T. R. Calhoun, E. L. Read, T.-K. Ahn, T. Mančal, Y.-C. Cheng, R. E. Blankenship, and G. R.

- Fleming, Evidence for wavelike energy transfer through quantum coherence in photosynthetic systems, Nature 446, 782 (2007).
- [34] Z. Hu, G. S. Engel, F. H. Alharbi, and S. Kais, Dark states and delocalization: Competing effects of quantum coherence on the efficiency of light harvesting systems, J. Chem. Phys. 148, 064304 (2018).
- [35] S. Tomasi, S. Baghbanzadeh, S. Rahimi-Keshari, and I. Kassal, Coherent and controllable enhancement of light-harvesting efficiency, Phys. Rev. A 100, 043411 (2019).
- [36] E. Z. Harush and Y. Dubi, Do photosynthetic complexes use quantum coherence to increase their efficiency? Probably not, Sci. Adv. 7, eabc4631 (2021).
- [37] M. Saberi, M. B. Harouni, R. Roknizadeh, and H. Latifi, Energy transfer and quantum correlation dynamics in FMO light-harvesting complex, Mol. Phys. 114, 2123 (2016).
- [38] M. Sarovar, A. Ishizaki, G. R. Fleming, and K. B. Whaley, Quantum entanglement in photosynthetic light-harvesting complexes, Nat. Phys. 6, 462 (2010).
- [39] J. T. Skolnik and D. A. Mazziotti, Cumulant reduced density matrices as measures of statistical dependence and entanglement between electronic quantum domains with application to photosynthetic light harvesting, Phys. Rev. A 88, 032517 (2013).
- [40] F. Fassioli and A. Olaya-Castro, Distribution of entanglement in light-harvesting complexes and their quantum efficiency, New J. Phys. 12, 085006 (2010).
- [41] R. Dutta and B. Bagchi, Delocalization and quantum entanglement in physical systems, J. Phys. Chem. Lett. 10, 2037 (2019).
- [42] S. Giannini, W.-T. Peng, L. Cupellini, D. Padula, A. Carof, and J. Blumberger, Exciton transport in molecular organic semiconductors boosted by transient quantum delocalization, Nat. Commun. 13, 2755 (2022).
- [43] A. G. Dijkstra and A. Beige, Efficient long-distance energy transport in molecular systems through adiabatic passage, J. Chem. Phys. 151, 034114 (2019).

- [44] R. E. Fenna and B. W. Matthews, Chlorophyll arrangement in a bacteriochlorophyll protein from *Chlorobium limicola*, Nature 258, 573 (1975).
- [45] E. Thyrhaug, K. žídek, J. Dostál, D. Bína, and D. Zig-mantas, Exciton structure and energy transfer in the Fenna–Matthews–Olson complex, J. Phys. Chem. Lett. 7, 1653 (2016).
- [46] D. E. Tronrud, J. Wen, L. Gay, and R. E. Blankenship, The structural basis for the difference in absorbance spectra for the FMO antenna protein from various green sulfur bacteria, Photosynth. Res. 100, 79 (2009).
- [47] N. Skochdopole and D. A. Mazziotti, Functional subsystems and quantum redundancy in photosynthetic light harvesting, J. Phys. Chem. Lett. 2, 2989 (2011).
- [48] See the Supplemental Material at http://link.aps.org/supple mental/10.1103/PRXEnergy.2.023002 for an explanation of the connection between the site basis set and the particle basis set, as well as additional data for calculations varying the degree of dephasing, the number of intrachromophore sites, the number of chromophores, and the strength of the interactions *V* and *ξ*. The Supplemental Material contains Figs. S1–S16 and Ref. [54].
- [49] F. Fassioli, A. Olaya-Castro, and G. D. Scholes, Coherent energy transfer under incoherent light conditions, J. Phys. Chem. Lett. 3, 3136 (2012).
- [50] C. Garrod and M. Rosina, Particle-hole matrix: Its connection with the symmetries and collective features of the ground state, J. Math. Phys. 10, 1855 (1969).
- [51] A. O. Schouten, L. M. Sager-Smith, and D. A. Mazziotti, Large cumulant eigenvalue as a signature of exciton condensation, Phys. Rev. B 105, 245151 (2022).
- [52] U. Fano, A common mechanism of collective phenomena, Rev. Mod. Phys. 64, 313 (1992).
- [53] G. D. Scholes, The Kuramoto-Lohe model and collective absorption of a photon, Proc. R. Soc. A 478, 20220377 (2022).
- [54] S. E. Smart, D. I. Schuster, and D. A. Mazziotti, Experimental data from a quantum computer verifies the generalized Pauli exclusion principle, Commun. Phys. 2, 11 (2019).